Electrochimica Acta 427 (2022) 140861

Contents lists available at ScienceDirect

Electrochimica Acta

journal homepage: www.journals.elsevier.com/electrochimica-acta

Catalytic electrodes for the oxygen reduction reaction based on co-doped (B-N, Si-N, S-N) carbon quantum dots and anion exchange ionomer

A.R. Nallayagari [a,b], E. Sgreccia [b], L. Pasquini [a], F. Vacandio [a], S. Kaciulis [c], M.L. Di Vona [b,*], P. Knauth [a,*]

[a] Aix Marseille University, CNRS, MADIREL (UMR 7246) and International Laboratory: Ionomer Materials for Energy, Campus St Jérôme, Marseille 13013, France
[b] Department of Industrial Engineering, International Laboratory, Ionomer Materials for Energy, University of Rome Tor Vergata, Roma 00133, Italy
[c] Institute for the Study of Nanostructured Materials, ISMN-CNR, Monterotondo Stazione, Roma 00015, Italy

ARTICLE INFO

Keywords:
Oxygen reduction
Carbon materials
Electrocatalyst
Fuel cells
Stability

ABSTRACT

B-N-, Si-N, and S-N-co-doped carbon quantum dots (CQD) were prepared by hydrothermal synthesis from inexpensive and non-toxic precursors. They were analysed by Raman, FTIR, and XPS spectroscopies and used as oxygen reduction reaction (ORR) electrocatalysts. The electrodes were prepared by drop-casting a slurry containing poly(sulfone trimethylammonium) hydroxide (PSU-TMA) to enhance the hydroxide-ion transport near the catalytically active centers. Furthermore, polyaniline (PANI), reported to be catalytically active for the ORR, was added to some electrodes. A similar trend was observed for the electrode capacitance measured by cyclovoltammetry in the non-Faradaic region and impedance spectroscopy. The ORR kinetics studied by linear sweep voltammetry showed the lowest onset and half-wave potentials and the lowest Tafel slopes for the B-N-co-doped samples, although the B concentration is low (0.5%). Data with and without PANI are quite similar. The S-N- and Si-N co-doped samples are slightly less efficient. The stability test demonstrated a decrease by about 10% of the diffusion-limited current after 500 cycles, indicating a microstructural change impacting the mass transport conditions, but the onset potential is not modified. Altogether, the good electrocatalytic activity of B-N-co-doped CQD with a low boron concentration in presence of PSU-TMA indicated the high potential of these electrodes. The inexpensive synthesis of co-doped CQD from non-toxic precursors is an important advantage of these materials vs other carbon-doped electrocatalysts.

1. Introduction

The sluggish kinetics of the oxygen reduction reaction (ORR), more than six orders of magnitude slower than the hydrogen oxidation reaction in acidic conditions, is a major concern for various energy storage and conversion devices, including metal air batteries and fuel cells [1,2]. The exceptionally high O=O bond energy (~500 kJ/mol) requires generally the use of noble-metal electrocatalysts, including platinum and palladium, for the four-electron reduction in acidic conditions [3–5], although some alternative non-noble materials were reported [6]. Polyaniline (PANI) was proposed as an interesting additive for catalytic electrodes [7,8], when the two-electron reduction is acceptable.

The ORR is however faster in alkaline medium [9] and non-noble electrocatalysts are applicable, including doped carbon materials [10–12]. The four-electron ORR to hydroxide ions can be written:

$$O_2 + 4\,e^- + 2\,H_2O \rightarrow 4\,HO^-\ E^\circ = 0.40\ V\ vs\ SHE \quad (1)$$

The two-electron ORR leads to the formation of hydrogenperoxide anions:

$$O_2 + 2\,e^- + H_2O \rightarrow HO_2^- + HO^-\ E^\circ = -0.07\ V\ vs\ SHE \quad (2)$$

The ratio of four-electron and two-electron reduction can be modified by the choice of the electrocatalyst. PANI was proposed for electrocatalytic electrodes in alkaline conditions in conjunction with carbon nanotubes or Pd; in the latter case, PANI is reported to prevent Pd nanoparticle agglomeration [13,14]. Various heteroatoms were studied as dopants in diverse carbonaceous materials, especially substitutional nitrogen, with sometimes surprisingly high enhancement of the catalytic activity [15–20]. Nanostructured carbons have especially retained the attention due to their solubility in organic solvents that make the drop-casting procedure available [18,21]. The electroactivity of carbon

* Corresponding authors.
E-mail addresses: divona@uniroma2.it (M.L. Di Vona), philippe.knauth@univ-amu.fr (P. Knauth).

https://doi.org/10.1016/j.electacta.2022.140861
Received 20 April 2022; Received in revised form 14 July 2022; Accepted 15 July 2022
Available online 16 July 2022
0013-4686/© 2022 Elsevier Ltd. All rights reserved.

quantum dots (CQD) for the ORR was demonstrated in 2012 [18]. CQD have a core composed of sp^2/sp^3 carbon atoms and oxygen/nitrogen-containing functional groups at the edges. We have recently compared the preparation of CQD by three different methods - pyrolysis, microwave irradiation and hydrothermal synthesis - and reported their respective properties [22]. The hydrothermal method is most promising due to the easily controllable composition and structure via the optimization of precursors and can produce CQD with uniform particle size [12]. We showed especially that the position of nitrogen atoms in the nanostructure, for example in graphitic, pyrrolic or pyridinic sites, changes significantly the properties of the CQD, including solubility, UV-vis absorption and fluorescence emission [22].

The incorporation of nitrogen on various sites inside the carbon nanostructure also modifies the catalytic properties [18,23]. Nitrogen-doped CQD are electrochemically active toward the ORR, but electrodes made with small CQD present a low electrical conductivity with high percolation threshold [24]. N is more electronegative than C; the electron-withdrawing ability of N makes neighbouring C atoms more positively charged, which facilitates the chemisorption of O_2 molecules. Co-doping by other heteroatoms, including B [24–26], Si [27] and S [28, 29], further enhances the electrocatalytic activity of nitrogen-doped carbons for the ORR. However, the sometimes labour-intensive, fastidious, and costly synthesis of carbon-based materials makes the large-scale implementation difficult [21].

In this work, we therefore investigate a simple and easily up-scalable synthesis of heteroatom co-doped CQD, using inexpensive starting materials and a fast hydrothermal synthesis procedure, which provides uniform CQD size [12]. The CQD are characterized by various techniques, including XPS, FTIR, and Raman spectroscopy.

The overpotential of the ORR contains the activation overpotential that can be reduced by the presence of a potent electrocatalyst improving the charge transfer kinetics, the Ohmic drop and the diffusion overpotential, related to the transport of oxygen gas and of hydroxide ions. Whereas the oxygen diffusion can be facilitated by the microstructure of the electrode, the hydroxide ion transport is enhanced by the presence of an anion exchange ionomer (AEI) in the electrode. The ORR occurs at the triple phase boundary between gas phase (pore), electron conducting catalyst (carbon paper/CQD) and hydroxide ion conductor (AEI), here poly(sulfone trimethylammonium hydroxide) (PSU-TMA) [30].

The electrodes investigated in this work are therefore prepared by drop-casting on carbon paper of a slurry containing co-doped CQD and AEI. Impedance spectroscopy and d.c. capacitance measurements are used to determine the electrochemically active surface area of the electrodes. The electrocatalytic activity for the ORR is studied in alkaline conditions (1 M KOH) by cyclic (CV) and linear sweep voltammetry (LSV) at various speeds of a rotating disk electrode (RDE).

2. Experimental

2.1. Materials

2-(2-Pyridylethyl)trimethoxysilane (Gelest) and polysulfone (MW = 55,500 g/mol, Solvay) were used without any further purification. L-cysteine (97%), sucrose (≥ 99.5%), boric acid (≥ 99.5%), polyaniline (emeraldine base, PANI-EB, MW >20,000 g/mol), dimethylformamide (DMF), and other chemicals were reagent-grade and were used as received from Sigma-Aldrich. Carbon paper (AvCarb EP55) and Pt/C 60% Cloth GDE (0.5 mg/cm^2) were obtained from the Fuel Cell Store.

2.2. Synthesis of CQD and PSU-TMA

2.2.1. N-doped CQD

The synthesis of N-doped CQD by a hydrothermal treatment was previously presented [19]. 0.45 g of glucosamine hydrochloride (2.1 mmol) was dissolved in 1 mL H_2O and 0.4 mL N-octylamine (2.1 mmol). The mixture was stirred for 50 min at 50 °C, then transferred in an autoclave and inserted into an oven at 190 °C for 12 h. The autoclave was then cooled down and the solid was dispersed in chloroform. The solution was centrifugated and the solid used for the electrode preparation.

Co-doped N-CQD were synthesized by the hydrothermal method starting from sucrose as carbon source. After the synthesis, the solutions were centrifugated at 8500 rpm during 10 min to eliminate any residue and dried at 85 °C. The detailed procedures are as follows.

2.2.2. B-N-CQD

B-N-CQD were prepared starting from 1.0 g (2.9 mmol) of sucrose and 5.0 mg (0.08 mmol) of boric acid (0.5 wt%) in 1 mL of H_2O. After dissolution, 4 mL DMF were added and the solution was stirred for about 30 min and heated in an autoclave at 190 °C for 12 h. The sample was soluble in DMF and DMSO.

2.2.3. Si-N-CQD

Si-N-CQD were prepared from a mixture of 0.5 g of sucrose (1.4 mmol) and 0.5 mL of 2-(2-pyridylethyl)trimethoxysilane (2.3 mmol) dissolved in 1 mL of H_2O. Then 4 mL DMF was added and the solution was stirred for 30 min and heated in an autoclave at 190 °C for 12 h. The sample was soluble in H_2O, DMF, and DMSO.

2.2.4. S-N-CQD

S-N-CQD were prepared from 0.5 g of sucrose (1.4 mmol) and 0.26 g of cysteine (2.1 mmol) dissolved in 1.5 mL of H_2O and 2 drops of 2 M HCl. Then 4 mL DMF was added and the solution was stirred for about 30 min and heated in an autoclave at 190 °C for 12 h. The sample was soluble in H_2O, DMF, and DMSO.

2.2.5. PSU-TMA

The ionomer was prepared via the chloromethylation route followed by the amination step. The detailed procedure was described in the Ref. [30]. In brief, chloromethylated-PSU (PSU-CM) was obtained using paraformaldehyde, trimethylchlorosilane, and $SnCl_4$ in chloroform. The above polymer was purified and its degree of chloromethylation was found to be 1.25. PSU-CM was then reacted with TMA in DMSO. The obtained PSU-TMA had a degree of amination of 0.96 and an ion exchange capacity (IEC) of 1.8 meq/g.

2.3. Slurry/ink and electrode preparation

2.3.1. CQD + PSU-TMA

For each electrode, (8 ± 1) mg of the anion exchange polymer (PSU-TMA) and (75 ± 5) mg of the respective co-doped CQD (B-N; Si-N; S-N) were dispersed in 0.5 mL DMF. The mixture was stirred overnight.

2.3.2. CQD + PANI + PSU-TMA

(8 ± 1) mg of PSU-TMA was mixed with (10 ± 1) mg of PANI-EB and (75 ± 5) mg of co-doped CQD, dispersed in 1 mL DMF and stirred overnight.

All ink solutions were deposited by the drop method: 5 μL of the above-prepared slurry was loaded on the surface of a carbon paper substrate and allowed to dry for 24 h at 80 °C.

2.4. Physicochemical characterization

2.4.1. Raman spectroscopy

FT-Raman spectra were collected using a Micro Raman imaging spectrometer, Optosky ATR 8300 with excitation wavelength of 785 nm. Spectra were collected for at least 10,000 scans using a laser power of 85 mW.

2.4.2. X-ray photoelectron spectroscopy (XPS)

The samples for XPS analyses were prepared by depositing a drop of

solution on a grated Au foil (purity 99.99%); then they were dried in air. Photoemission spectra were acquired using a spectrometer Escalab 250Xi (Thermo Fisher Scientific Ltd., East Grinstead, UK) with a monochromatic Al Kα (1486.6 eV) excitation source and six-channeltron detection system. All spectra were collected at pass energy of 40 eV in standard mode of electromagnetic lens system corresponding to an analysis area of approximately 1 mm in diameter. The binding energy (BE) scale was corrected for a low static charging by positioning the C 1 s peak of aliphatic carbon (C—C, C—H bonds) at BE = 285.0 eV and controlling if the Fermi level is positioned at BE = 0 eV. Spectroscopic data were processed by the Avantage v.5 software (Thermo Fisher Scientific Ltd).

2.4.3. FTIR spectroscopy

The FTIR spectra were recorded between 500 and 4000 cm^{-1} using a Perkin Elmer Spectrum 2 IR spectrometer (Waltham, Massachusetts, United States) equipped with an ATR crystal diamond module.

2.4.4. Electrochemical measurements

In all the electrochemical experiments, a conventional three-electrode set up was used with a glassy carbon rotating disk electrode with 0.07 cm^2 area (RDE, OrigaTrod, OrigaLys) as working electrode. The coated carbon paper samples were fixed on the glassy carbon disk. A 4 cm^2 platinum foil was the counter-electrode and Ag/AgCl (KCl saturated) served as reference electrode ($E = 0.197$ V vs SHE). 1 M KOH was used as an electrolyte, which was saturated with oxygen by gently bubbling pure O_2 through the solution for at least 40 min. Cyclic voltammetry (CV), linear sweep voltammetry (LSV) and electrochemical impedance spectroscopy (EIS) measurements were performed at room temperature using a BioLogic VMP3 apparatus. The scan rates for the CV and the LSV measurements were 20–100 mV/s and 5 mV/s respectively with various rotating speeds of the RDE between 500 and 2000 rpm. The long-term cycling tests were performed between −0.3 and −0.7 V vs Ag/AgCl at 1500 rpm with 50 mV/s scan rate. The impedance spectra were recorded with an a.c. amplitude of 20 mV in a frequency range between 1 Hz and 1 MHz.

3. Results

3.1. synthesis and characterization of co-doped CQD

The hydrothermal reaction was carried out starting from sucrose and different molecular precursors of the doping elements. In the case of B-N-CQD, the source of nitrogen in the CQD framework was attributed to the decomposition of DMF [31,32]. Scheme 1 shows a simplified representation of the structure of the doped CQD based on the results of various characterizations.

Fig. 1 shows the Raman spectrum of B-N-CQD with the typical D and

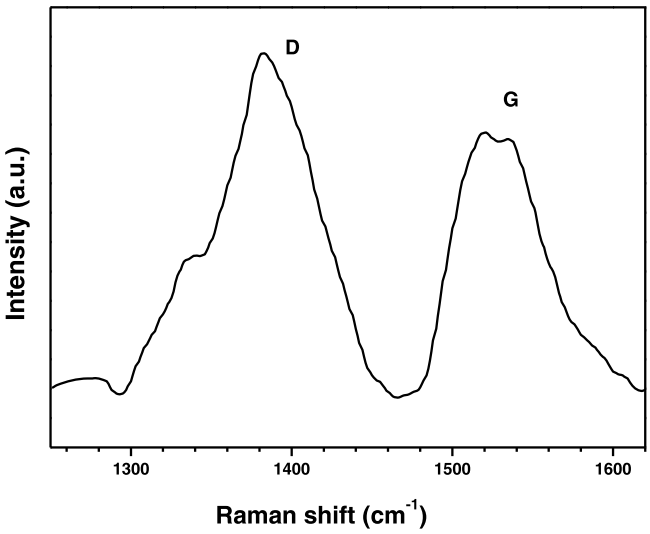
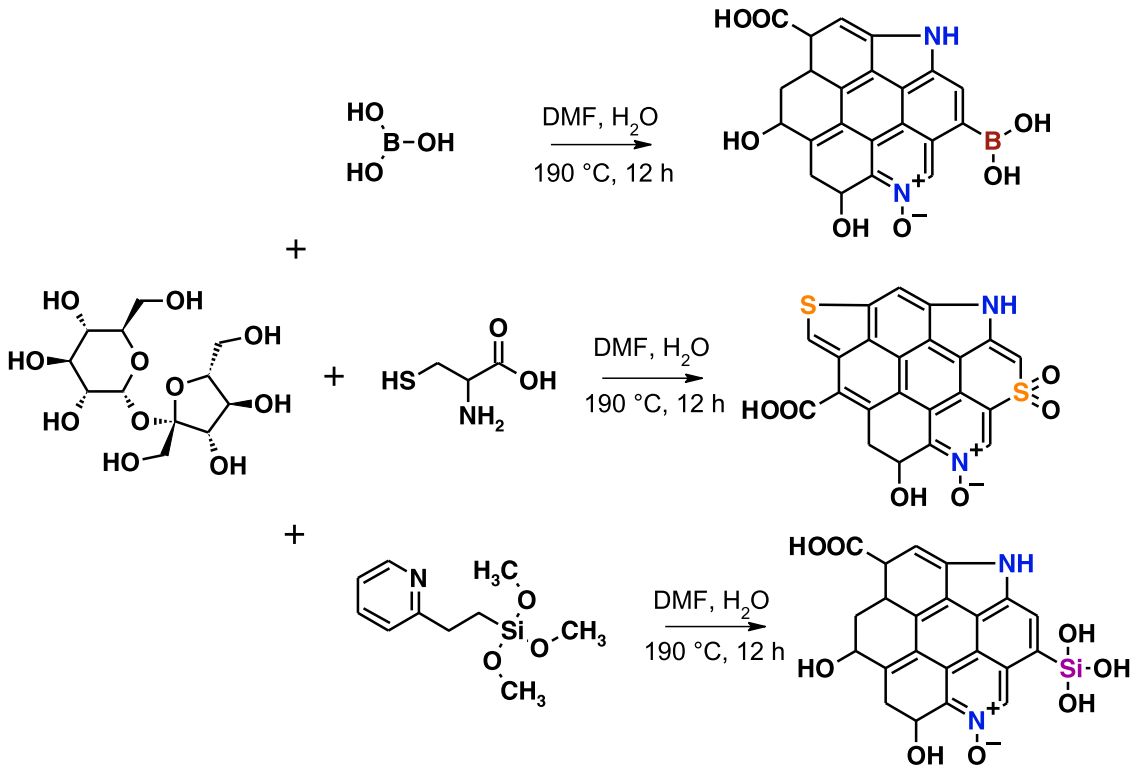


Fig. 1. Raman spectrum of B-N-CQD.



Scheme 1. Schematic representation of B-N, S-N and Si-N co-doped CQD obtained by the hydrothermal route.

G bands [33]. The D line is associated with "disorder peaks" that are related to the defects in amorphous carbons. The intensity of the D band in CQD can be connected with the presence of a high ratio of "C-edge" that induces defects in the structure or more generally to structural modifications such as the presence of a doping atom [34,35]. The G band is related to sp^2 carbon in double bonds and aromatic rings. The positions of D and G bands are similar for all samples (Figs. S1 and S2). The relative intensity of D and G bands is related to the size and the defect density (D band) and ultimately to the edge ratio [35,36]. In our samples the I_D/I_G value is around 1.3, which is in agreement with the literature and indicates a relatively high edge over graphene ratio [35,37]; this value might be attributed to the additional doping by B, Si or S [38]. It must also be considered that the excitation wavelength ($\lambda = 785$ nm) can affect the peak position and intensity, especially for the G band, which leads to an overestimation of the ratio values [39].

Fig. 2 shows the FTIR spectra of the doped samples. Adsorptions in the region 3000–3500 cm^{-1} originate from the O—H stretching vibration and are more intense for S- and Si-N-CQD. The solubility of S and Si doped samples in water confirms their greater hydrophilicity which was attributed, for S doped carbon materials, to the electrostatic interactions of C-SO_x-C moieties with the surrounding molecules [40]. Narrow peaks in the range of 2930–2940 cm^{-1} belong to N—H and C—H stretching, while signals around 1690 and 1590 cm^{-1} are attributed to C═O and C═C stretching adsorptions. At 1150 cm^{-1} the C—N stretching is observed for all samples. B-N-doped CQD (black spectrum) shows a distinct band around 1370 cm^{-1} corresponding to B-O and B-OH groups vibrations [41]. A sharp peak at 940 cm^{-1} and a broad signal at 1065 cm^{-1} are related to Si-C and Si-O adsorption of Si-N-CQD (blue spectrum). The S-N-doped sample (red spectrum) shows a broad signal at 1070 cm^{-1} belonging to S═O groups [42]. The thiophene ring vibration can be seen at 1450 cm^{-1}.

Fig. 3 shows the XPS spectra of the doping atoms with the peak fitting. C 1 s regions and survey spectra are reported in the Supplementary Information. The amount of dopants and their chemical bonding in the CQD are summarized in Table 1.

Nitrogen is present in all the samples as pyrrolic (N 1 s A) and pyridinic oxide (N 1 s B) with a higher percentage of dopants for the Si-N and S-N CQD, where a nitrogen-containing precursor is provided. Whereas pyrrolic N is predominating in B-N and S-N samples, pyridinic oxide bonds are predominant in Si-N CQD. The lower content of B and Si vs S is related to the molecular structure of the precursors, where the dopant atom is bound to -OR ligands.

For B-N-CQD, the region B 1 s indicates the presence of borinic boron (C-B-O_2 species) [25,43]. As already reported, the B atom seems therefore to be located at the edge of the CQD framework [26] (Fig. 3a).

In S-N-CQD, the S 2p A signal can be deconvoluted into spin-orbit doublet (S $2p_{3/2}$ and S $2p_{1/2}$ peaks) at 163.8 and 165.1 eV, like in thiophene structures (-C-S-C-) [10]. The S 2p B signal at 167.4 (S $2p_{2/3}$) and 169.1 eV (S $2p_{1/2}$) can be assigned to -C-SO_x-C groups [28,44], confirming the insertion of sulphur in the CQD (Fig. 3b).

Si-N-CQD presents in the region Si 2p a signal at 102.5 eV ascribed to C–Si–O chemical bonds, probably indicating an edge functionalization of CQD [27,45] (Fig. 3c). The qualitative atom size comparison shown in Fig. 3d supports that B, Si and S are placed at edge sites in the CQD, because these heteroatoms are larger than carbon.

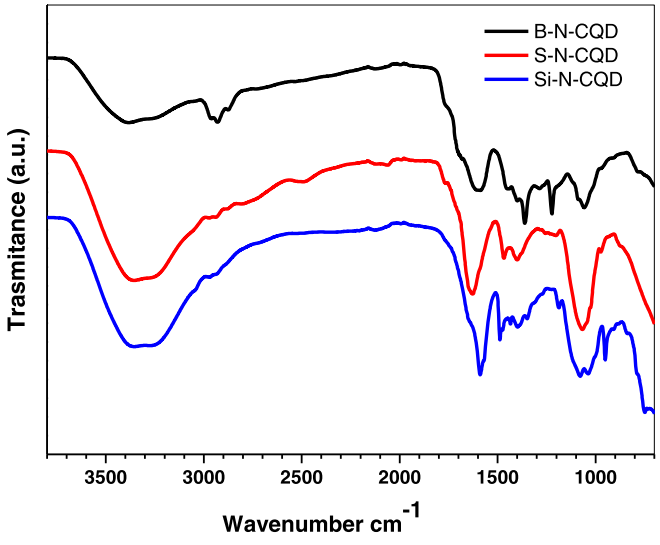


Fig. 2. FTIR spectra of co-doped CQD.

3.2. Electrode capacitance measurements

Electrode capacitances were measured by cyclovoltammetry (CV) and by impedance spectroscopy (IS).

Fig. 4a shows typical CV curves for different scan rates of a B-N-CQD + PSU-TMA electrode in the non-Faradaic region. The electrode capacitances can be calculated from the linear relation between the current density j and the scan rate dU/dt (Fig. 4b):

$$j = C \cdot \frac{dU}{dt} \tag{3}$$

Similar measurements for other electrodes are reported in the Supporting Information. Average capacitance values for all samples are given in Table 2. Using the geometrical electrode area of the samples, the areal capacitances would be between 4.1 and 8.4 mF cm^{-2}.

Impedance spectra of electrodes containing Si-N-CQD are shown in Fig. 5. The spectra for other electrodes are shown in the Supporting Information.

The impedance spectra of all electrodes can be described by an equivalent circuit of a resistance R, representing essentially the electrode resistance, in series with a constant phase element (CPE), associated to the electrode capacitance. The impedance Z of a CPE can be written:

$$Z(CPE) = \frac{1}{Y}(i\omega)^{-m} \tag{4}$$

In this equation, i is the imaginary unit, ω the angular frequency, Y the CPE value and m the characteristic CPE exponent. For m near 1, the CPE can be considered an imperfect capacitance with value Y. The best fit results for R, Y and m are reported in Table 2. One can observe that the electrode capacitances determined by CV measurements show a similar trend with the values of Y measured by impedance spectroscopy. The sample resistance increases for both groups of samples in the order B < Si < S, whereas the capacitances and Y decrease in this order. Both results can be related to an increased aggregation of CQD in the order B < Si < S that reduces the electrochemically active surface area.

There exists a relation between m and the fractal dimension D of the electrodes [46]:

$$m = \frac{1}{D-1} \tag{5}$$

The average fractal dimension is in the order of $D = 2.4$ in agreement with the porous electrode morphology.

3.3. ORR kinetics and Koutecky-Levich plots

Fig. 6 shows cyclovoltammograms of N-CQD+PSU-TMA electrodes without co-doping in oxygen-saturated 1 M KOH and in a solution purged by nitrogen flux. Whereas a cathodic current is absent in the latter case, one recognizes a strong reduction peak with an onset potential around −0.2 V vs Ag/AgCl when oxygen is present, showing the electroactivity of N-doped CQD for the ORR.

LSV curves at various rotating speeds are shown for B-N, Si-N and S-N co-doped CQD in Fig. 7. Onset and half-wave potentials determined at

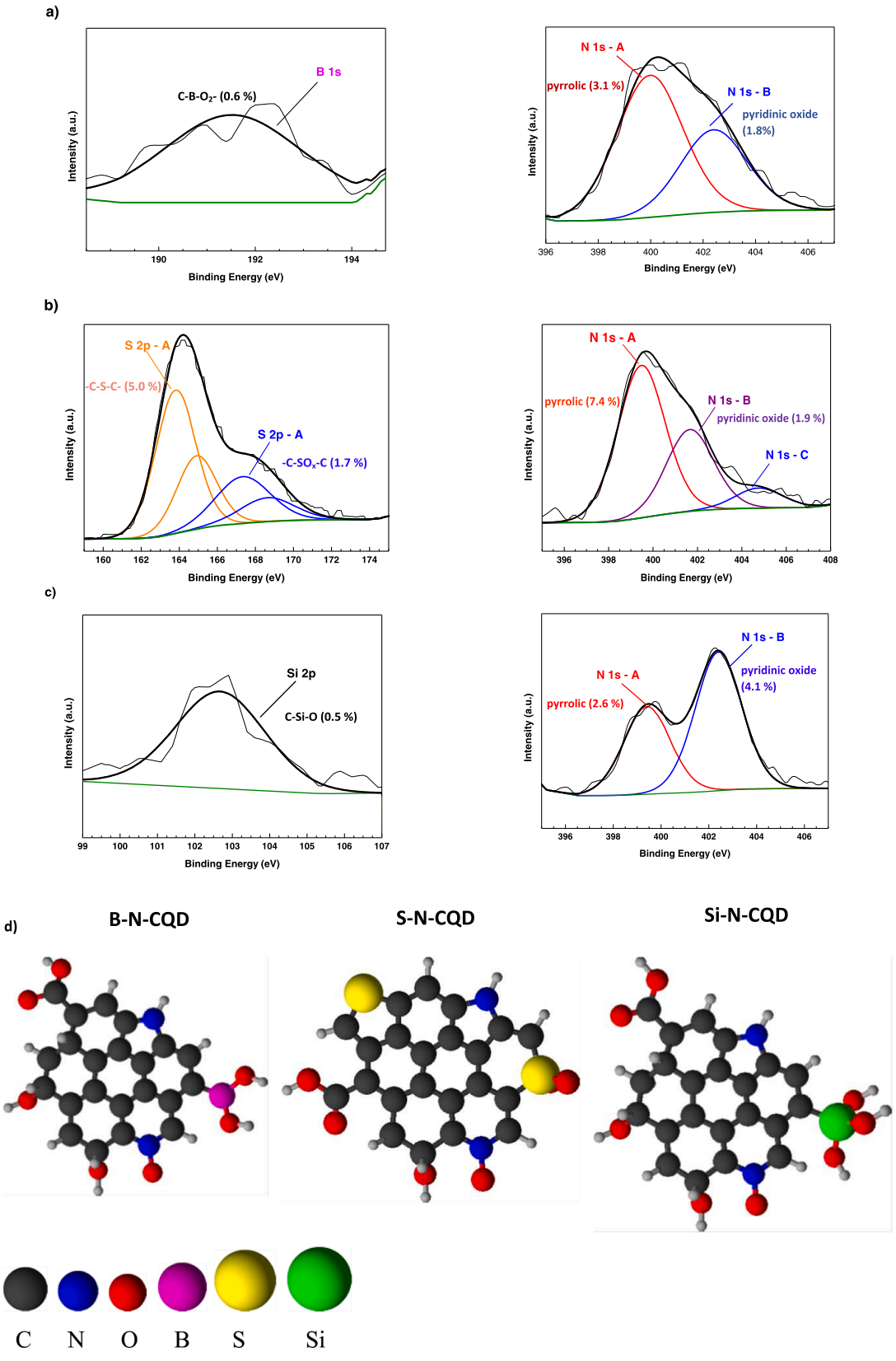


Fig. 3. XPS spectra of the B 1 s, S 2p, Si 2p, and N 1 s regions for (a) B-N, (b) S-N, (c) Si-N co-doped samples, (d) schematic representation of CQD with atom sizes.

1500 rpm from these curves are reported in Table 3.

One notices a current plateau around −0.5 V vs Ag/AgCl for all electrodes. The current values in this region can be used to determine the number of exchanged electrons using the Koutecky-Levich equation between the current j and the rate of the rotating-disk electrode ω [47, 48]:

Table 1
Dopant atomic concentration and chemical bonding in co-doped CQD.

CQD	Heteroatom chemical bonding and atomic concentration	Nitrogen chemical bonding and atomic concentration
B-N	C-B-O_2: 0.6%	Pyridinic oxide: 1.8% Pyrrolic: 3.1%
S-N	C-S-C: 5.0% C-SO_x-C: 1.7%	Pyridinic oxide: 1.9% Pyrrolic: 7.4%
Si-N	C-Si-O: 0.5%	Pyridinic oxide: 4.1% Pyrrolic: 2.6%

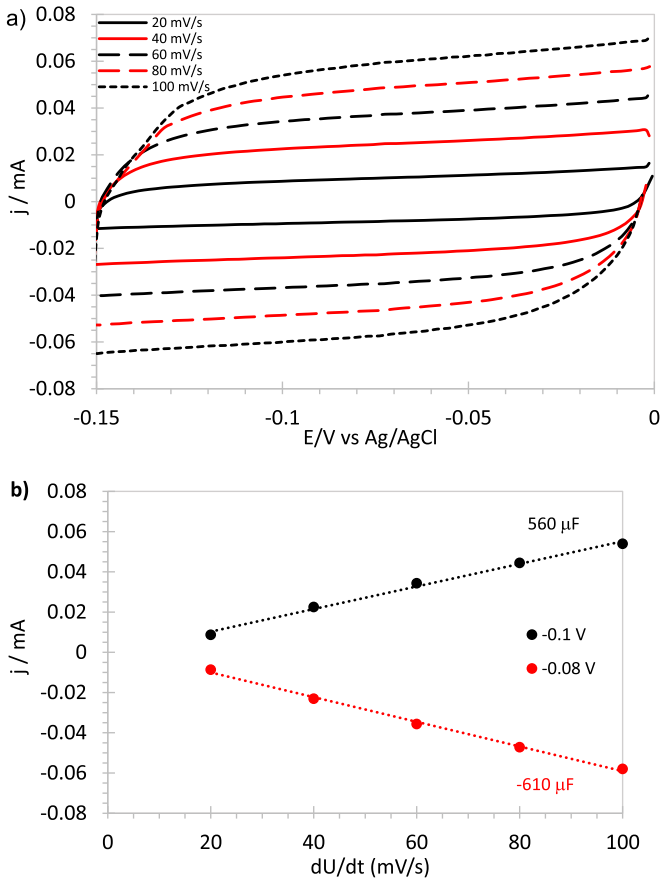


Fig. 4. Capacitance measurements of B-N-CQD + PSU-TMA electrode. (a) CV curves at different scan rates and (b) linear plots of current vs scan rate for different potential values.

Table 2
Capacitance *C* from CV, resistance *R*, value *Y* and exponent *m* of constant phase element of various electrodes with co-doped CQD.

Sample	*C (µF)*	*R (Ω)*	*Y (μFs^{n-1})*	*m*
B-N-CQD + PSU-TMA	590	8.8	790	0.76
Si-N-CQD + PSU-TMA	380	13.2	690	0.78
S-N-CQD + PSU-TMA	290	22.7	520	0.79
B-N-CQD + PANI + PSU-TMA	370	6.2	1430	0.68
Si-N-CQD + PANI + PSU-TMA	350	14.0	1130	0.69
S-N-CQD + PANI + PSU-TMA	350	16.5	710	0.69

$$\frac{1}{j} = \frac{1}{j_k} + \frac{1}{B \cdot \omega^{1/2}} \quad (6)$$

In this equation, j_k is the kinetic current and B is the Levich slope, which is given by the relation:

$$B = 0.62 \cdot A \cdot n \cdot F \cdot c(O_2) \cdot D(O_2)^{\frac{2}{3}} \cdot \nu^{-\frac{1}{6}} \quad (7)$$

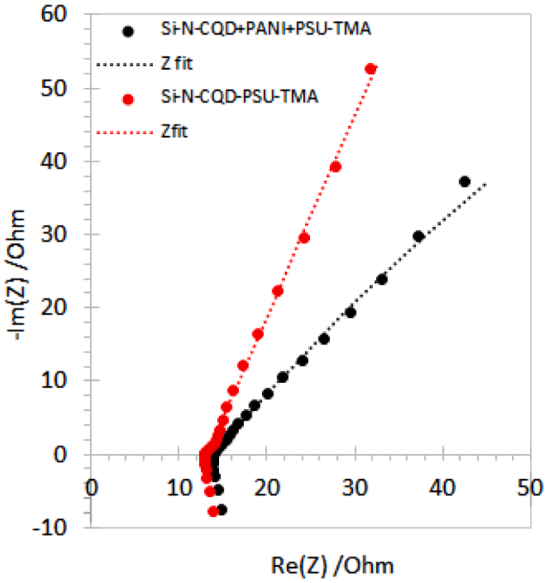


Fig. 5. Impedance spectra of Si-N-CQD containing electrodes with corresponding Zfit plot.

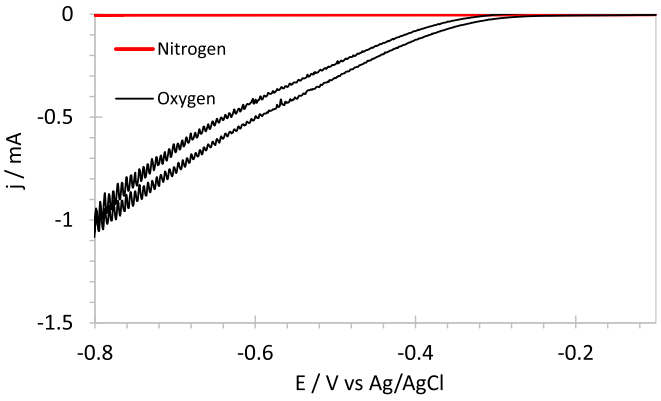


Fig. 6. Comparison of cyclovoltammetric curves with N—CQD + PSU-TMA in oxygen-saturated solution (black curve) and in nitrogen-saturated solution (red curve).

Here, *A* is the geometrical electrode area, *n* the number of exchanged electrons, *F* the Faraday constant (96,485 C.mol^{-1}), $c(O_2)$ the saturation concentration of oxygen in 1 M KOH (9×10^{-7} mol cm^{-3} [49]), $D(O_2)$ the oxygen diffusion coefficient in 1 M KOH (1.5×10^{-5} cm^2 s^{-1} [50]), and ν the kinetic viscosity of the 1 M KOH solution (0.0094 cm^2 s^{-1}) [51].

Typical Koutecky-Levich plots are shown in Fig. 8 for B-N co-doped CQD+PANI+PSU-TMA at potentials between −0.4 and −0.55 V. As expected, the slope decreases with increasing cathodic potential corresponding to an increase of the number of exchanged electrons, from n = 3.5 at −0.4 V to 4.0 at E = −0.5 V vs Ag/AgCl (Table 3). This result confirms that co-doped CQD-based electrodes catalyse the four-electron ORR, as previously shown by other authors [18].

Fig. 9 shows the current density of various CQD-based electrodes in comparison with a benchmark commercial Pt/C cloth. The current density at −0.7 V vs Ag/AgCl and 2000 rpm of the benchmark is near the diffusional limiting current density calculated according to the Levich Eq. (7) (j_{lim} = 4.1 mA/cm^2); the current density of CQD reaches 2 mA/cm^2 under these conditions.

In order to facilitate the comparison with literature data, the onset and half-wave potentials of ORR are expressed in the following vs the reversible hydrogen electrode (RHE), which potential is calculated from the potentials E vs the Ag/AgCl electrode according to the equation:

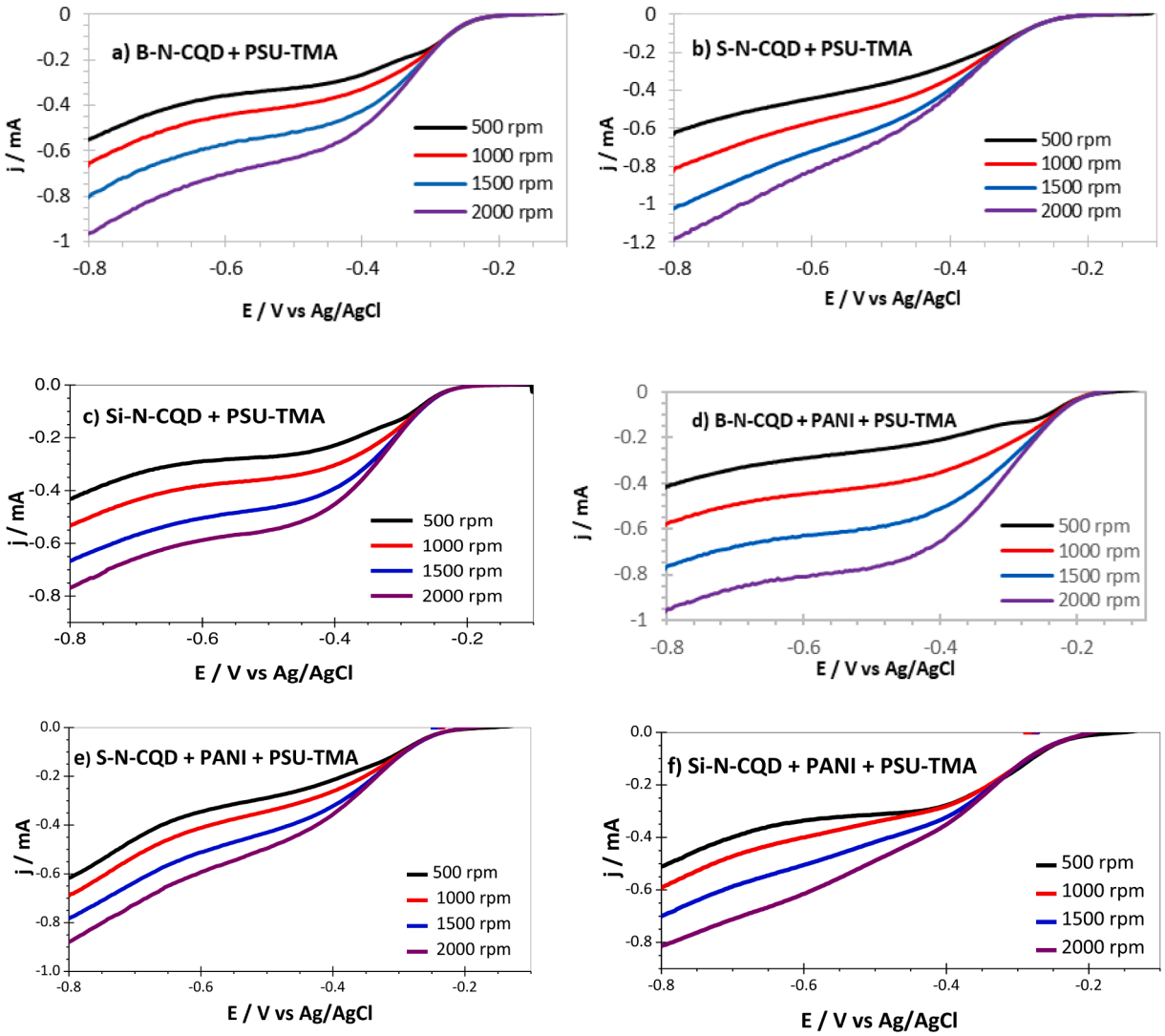


Fig. 7. LSV curves for co-doped CQD + PSU-TMA electrodes (a–c) and CQD + PANI + PSU-TMA electrodes (d–f).

Table 3
Electrochemical properties of co-doped ORR electrodes: onset potential E_{onset}, half-wave potential $E_{1/2}$, number of exchanged electrons n at E = 523 mV vs RHE, and Tafel slope B (see text).

Electrode	E_{onset} vs RHE/ mV	$E_{1/2}$ vs RHE/ mV	n	B / mV
B-N-CQD + PSU-TMA	849	711	4	68
Si-N-CQD + PSU-TMA	849	711	4	73
S-N-CQD + PSU-TMA	840	685	4	82
B-N-CQD + PANI + PSU-TMA	858	730	4	68
Si-N-CQD + PANI + PSU-TMA	827	703	4	99
S-N-CQD + PANI + PSU-TMA	831	699	4	85

$$E_{RHE}\ /mV\ = E_{Ag/AgCl} + 59 * pH + 197 \quad (8)$$

One can notice that B-N co-doped CQD show the highest onset and half-wave potentials, indicating the best electrocatalytic activity.

3.4. Tafel plots

Fig. 10 shows Tafel plots for the different electrodes. The respective

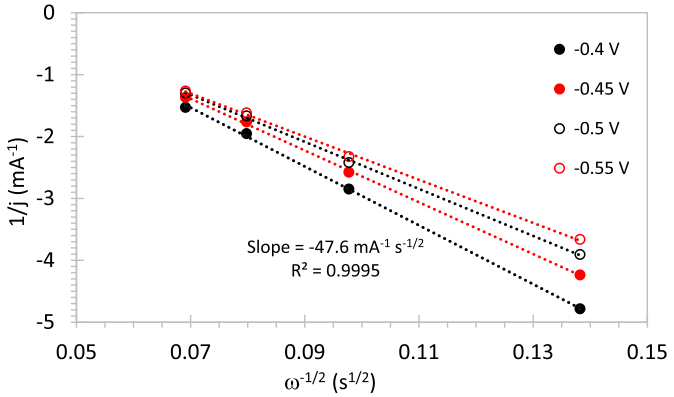


Fig. 8. Koutecky-Levich plots for B-CQD + PANI + PSU-TMA at various potentials.

Tafel slopes are reported with other relevant electrocatalytic performance data in Table 3.

One can notice that in both Tafel diagrams the B-N-co-doped samples show the lowest Tafel slope, which can be attributed to a better electrocatalytic performance. The slope is near the value expected for a rate-

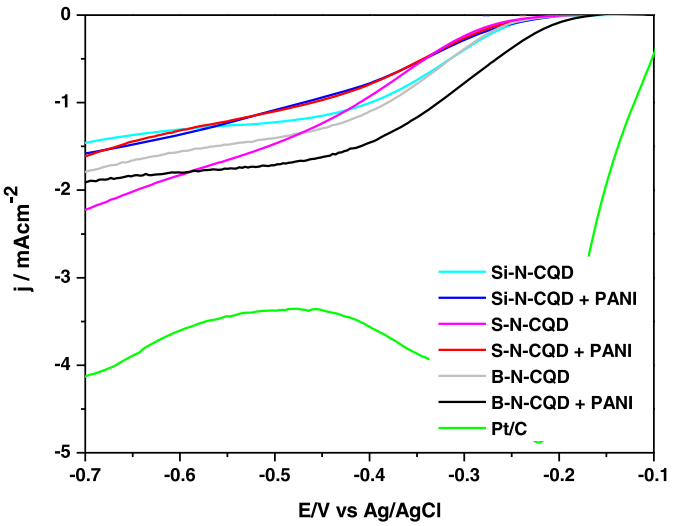


Fig. 9. Current density at 2000 rpm of co-doped CQD in comparison with Pt/C cloth.

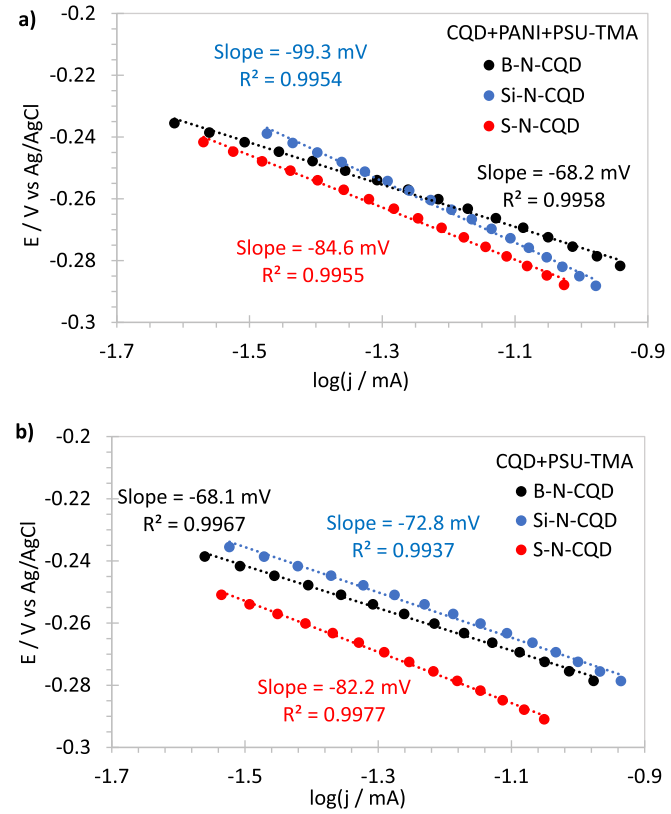


Fig. 10. Tafel plots for (a) co-doped CQD + PANI + PSU-TMA, (b) co-doped CQD + PSU-TMA at 1500 rpm.

determining pseudo two-electron reduction. S-N-co-doped samples present in both cases a higher Tafel slope in the order of 84 mV, intermediate between literature values at low and high current densities. The Si-N-co-doped samples show a large discrepancy of slopes, but the sample without PANI has an interestingly low value.

3.5. Stability test

Fig. 11 shows the stability test of a Si-N-CQD+PSU-TMA electrode

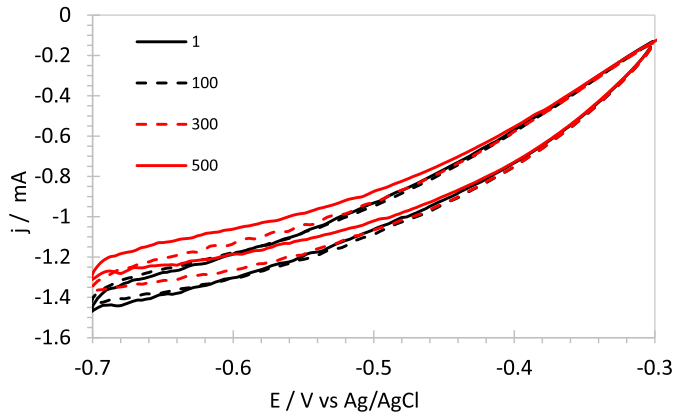


Fig. 11. Stability test of Si-N-CQD + PSU-TMA electrode over 500 cycles (dU/dt = 50 mV/s).

over 500 cycles. One can observe a decrease of the current in the transport-dominated region by about 10% indicating an electrode morphology change that modifies mass transport conditions, but the onset potential, indicative of the electrocatalytic properties, remains constant over the cycles.

4. Discussion

The data in Table 3 show that the B-N-co-doped samples have overall the best electrocatalytic properties with the lowest Tafel slopes and the most positive onset and half-wave potentials, followed by Si-N and S-N. This is a remarkable result because these electrodes contain only a small amount of B, confirming literature observations of the high efficiency of B-N co-doped carbon ORR electrodes [21,24–26]. Although samples containing PANI have globally more positive half-wave potentials, their Tafel slopes are higher so that no distinct advantage can be found using PANI. Future work will therefore be focused on samples without PANI.

A comparison of onset and half-wave potentials with the literature [15] for various doped carbon materials (Table 4) shows slightly lower performance for the B-N co-doped samples, whereas the data for Si-N and S-N co-doped CQD are in good agreement with reference data.

The electroactivity of co-doped CQD is related to the availability of chemisorption sites for oxygen molecules and the weakening of the O═O bond. The creation of an electron density asymmetry and local structural distortions, due to heteroatom size mismatch, alters the electroactivity. Defects of CQD include single/multiple vacancies, edge sites, dangling groups, and dislocations, which tend to change the local electronic states and bond lengths; defects have strong chemisorption and chemical affinity for various molecules. Furthermore, CQD have plenty of oxygenated functional groups (e.g. -OH and -COOH) that

Table 4
Comparison of electrocatalytic performances of various doped carbon materials.

Electrode	E_{onset} vs RHE / V	$E_{1/2}$ vs RHE/ V	Refs.
B-N-CQD + PSU-TMA	0.85	0.71	This work
B-N-CQD + PANI + PSU-TMA	0.86	0.73	This work
B-N-doped nanodiamond	0.93	0.81	[52]
B-N-doped GQD/graphene	0.91	0.76	[53]
B-N-doped carbon nanotubes	0.91	0.76	[54]
Graphene/B-doped CQD	0.94	0.73	[26]
Si-N-CQD + PSU-TMA	0.85	0.71	This work
Si-N-CQD + PANI + PSU-TMA	0.83	0.70	This work
Si-N-doped carbon nanospheres	0.85	–	[27]
S-N-CQD + PSU-TMA	0.84	0.69	This work
S-N-CQD + PANI + PSU-TMA	0.83	0.70	This work
S-N-doped graphene	0.89	–	[55]
S-N-doped graphene	0.83	–	[56]
S-N-doped carbon nanotubes	0.96	0.81	[57]

modify the local electron density and provide additional active sites for electrochemical reactions; they can also enhance the electrode wettability by the electrolyte. The amount and type of surface groups can be customized by the choice of reactants and synthesis conditions. However, a too large density of oxygenated groups reduces the conductivity of CQD and hinders the interfacial electron transfer.

Heteroatom doping generally causes structural distortion and charge redistribution in neighbouring C atoms, which alters the local electronic structure and density of states, which promotes the adsorption and desorption of reactants and intermediates benefiting the ORR. The partial positive charge of B atoms due to their lower electronegativity than C and their position of C-BO_2 edge sites facilitate the adsorption of O_2 molecules [21]. Graphite-like BC3, substituting B atoms for C atoms, can ameliorate the in-plane electron transfer and generate polarized sites as catalytically active centers [26]. The doping by Si enhances the catalytic activity of carbon nanomaterials [27]; density functional theory calculations indicated that the carbon atoms neighbouring silicon acquire a partial negative charge in graphene sheets, which changes the chemisorption mode of O_2 molecules from the usual end-on adsorption on graphene surfaces to side-on adsorption on Si-doped or Si-N-co-doped samples, also supported by the large atomic radius of Si. Furthermore, the electrons in Si-doped graphene are more easily transferred to O_2 [27]. Both factors evidently facilitate the ORR. Sulfur has a large atomic radius and an electronegativity close to carbon; the enhanced ORR electroactivity of S-doped graphene is attributed to modifications of electron density [38].

Co-doped CQD show an elevated ORR activity due to synergistic coupling effects between heteroatoms and a substantially enhanced electron density [38]. In our work, the highest ORR electrocatalytic activity is observed B-N co-doped CQD. However, B and N tend to exist as pairs when the doping content is too high, which are inactive towards the ORR [24]. Furthermore, excessive B and N doping decreases the electrical conductivity of CQD, which contributes to the ORR electroactivity degradation [24]. For this reason, the B content was voluntarily limited in our electrodes, also given the high reactivity of boric acid in hydrothermal conditions. The hydrophilicity of the doped CQD can affect the performances inducing higher wettability or aggregation of the catalyst. C-SOx groups present in S-doped carbon material can interact with oxygen atoms and increase catalyst aggregation, reducing its activity [40].

Finally, one should emphasize that the electrodes presented in this work are prepared with an efficient low cost and low environmental impact synthesis starting from non-toxic and inexpensive precursors, which is a competitive advantage.

5. Conclusions

B-N-, S-N- and Si-N-co-doped CQD were prepared by hydrothermal synthesis using inexpensive and non-toxic precursors. They were analysed by Raman, FTIR, and XPS spectroscopy and used as electrocatalysts for the ORR in alkaline conditions. The electrode slurries were prepared by mixing with a hydroxide-conducting ionomer PSU-TMA to facilitate the hydroxide ion transport near the catalytically active centers. In the other electrode family, PANI which presents itself a catalytic activity for the ORR, was also added. The slurry was then drop-cast on carbon paper. The electrochemical ORR tests showed the best electrocatalytic properties for electrodes containing B-N-co-doped CQD, although the amount of boron is low, confirming the excellent performance of B-N-co-doped carbon materials. The inexpensive and environmentally friendly synthesis procedure is a competitive advantage of the ORR electrodes reported in this work.

CRediT authorship contribution statement

A.R. Nallayagari: Investigation, Writing – original draft. **E. Sgreccia:** Validation, Data curation, Supervision. **L. Pasquini:** Validation, Data curation. **F. Vacandio:** Validation, Data curation. **S. Kaciulis:** Validation, Data curation. **M.L. Di Vona:** Conceptualization, Writing – review & editing. **P. Knauth:** Conceptualization, Writing – review & editing.

Declaration of Competing Interest

The authors declare that they have no known competing financial interests or personal relationships that could have appeared to influence the work reported in this paper.

Data availability

The data that has been used is confidential.

Supplementary materials

Supplementary material associated with this article can be found, in the online version, at doi:10.1016/j.electacta.2022.140861.

References

[1] R. Ma, G. Lin, Y. Zhou, Q. Liu, T. Zhang, G. Shan, M. Yang, J. Wang, A review of oxygen reduction mechanisms for metal-free carbon-based electrocatalysts, npj Comput. Mater. 5 (1) (2019) 78.
[2] X. Tian, X.F. Lu, B.Y. Xia, X.W. Lou, Advanced Electrocatalysts for the oxygen reduction reaction in energy conversion technologies, Joule 4 (1) (2020) 45–68.
[3] S.Y. Cha, W.M. Lee, Performance of proton exchange membrane fuel cell electrodes prepared by direct deposition of ultrathin platinum on the membrane surface, J. Electrochem. Soc. 146 (11) (1999) 4055–4060.
[4] H.A. Gasteiger, S.S. Kocha, B. Sompalli, F.T. Wagner, Activity benchmarks and requirements for Pt, Pt-alloy, and non-Pt oxygen reduction catalysts for PEMFCs, Appl. Catal. B Environ. 56 (1–2) (2005) 9–35.
[5] M.S. Wilson, J.A. Valerio, S. Gottesfeld, Low platinum loading electrodes for polymer electrolyte fuel-cells fabricated using thermoplastic ionomers, Electrochim. Acta 40 (3) (1995) 355–363.
[6] F. Jaouen, E. Proietti, M. Lefevre, R. Chenitz, J.P. Dodelet, G. Wu, H.T. Chung, C. M. Johnston, P. Zelenay, Recent advances in non-precious metal catalysis for oxygen-reduction reaction in polymer electrolyte fuel cells, Energy Environ. Sci. 4 (1) (2011) 114–130.
[7] C. Coutanceau, M.J. Croissant, T. Napporn, C. Lamy, Electrocatalytic reduction of dioxygen at platinum particles dispersed in a polyaniline film, Electrochim. Acta 46 (4) (2000) 579–588.
[8] G. Wu, K.L. More, C.M. Johnston, P. Zelenay, High-performance electrocatalysts for oxygen reduction derived from polyaniline, iron, and cobalt, Science 332 (6028) (2011) 443–447.
[9] A. Damjanovic, M.A. Genshaw, J.O.M. Bockris, The mechanism of oxygen reduction at platinum in alkaline solutions with special reference to H_2O_2, J. Electrochem. Soc. 114 (11) (1967) 1107.
[10] J.E. Park, Y.J. Jang, Y.J. Kim, M.S. Song, S. Yoon, D.H. Kim, S.J. Kim, Sulfur-doped graphene as a potential alternative metal-free electrocatalyst and Pt-catalyst supporting material for oxygen reduction reaction, PCCP 16 (1) (2014) 103–109.
[11] R.G. Ma, G.X. Lin, Y. Zhou, Q. Liu, T. Zhang, G.C. Shan, M.H. Yang, J.C. Wang, A review of oxygen reduction mechanisms for metal-free carbon-based electrocatalysts, npj Comput. Mater. 5 (2019) 15.
[12] X. Wang, Y.Q. Feng, P.P. Dong, J.F. Huang, A mini review on carbon quantum dots: preparation, properties, and electrocatalytic application, Front. Chem. 7 (2019) 9.
[13] H.J. Zhou, Y.Q. Lin, P. Yu, L. Su, L.Q. Mao, Doping polyaniline with pristine carbon nanotubes into electroactive nanocomposite in neutral and alkaline media, Electrochem. Commun. 11 (5) (2009) 965–968.
[14] M.S. Matseke, T.S. Munonde, K. Mallick, H.T. Zheng, Pd/PANI/C Nanocomposites as electrocatalysts for oxygen reduction reaction in alkaline media, Electrocatalysis 10 (4) (2019) 436–444.
[15] X.M. Ge, A. Sumboja, D. Wuu, T. An, B. Li, F.W.T. Goh, T.S.A. Hor, Y. Zong, Z. L. Liu, Oxygen reduction in alkaline media: from mechanisms to recent advances of catalysts, ACS Catal. 5 (8) (2015) 4643–4667.
[16] W. Ding, Z. Wei, S. Chen, X. Qi, T. Yang, J. Hu, D. Wang, L.J. Wan, S.F. Alvi, L. Li, Space-confinement-induced synthesis of pyridinic- and pyrrolic-nitrogen-doped graphene for the catalysis of oxygen reduction, Angew. Chem. Int. Ed. 52 (45) (2013) 11755–11759.
[17] D.W. Wang, D.S. Su, Heterogeneous nanocarbon materials for oxygen reduction reaction, Energy Environ. Sci. 7 (2) (2014) 576–591.
[18] Q.Q. Li, S. Zhang, L.M. Dai, L.S. Li, Nitrogen-doped colloidal graphene quantum dots and their size-dependent electrocatalytic activity for the oxygen reduction reaction, J. Am. Chem. Soc. 134 (46) (2012) 18932–18935.
[19] L. Tian, X.H. Zhai, X. Wang, X.L. Pang, J. Li, Z. Li, Morphology and phase transformation of alpha-MnO_2/MnOOH modulated by N-CDs for efficient

electrocatalytic oxygen evolution reaction in alkaline medium, Electrochim. Acta 337 (2020), 135823.
[20] A. Sarapuu, E. Kibena-Poldsepp, M. Borghei, K. Tammeveski, Electrocatalysis of oxygen reduction on heteroatom-doped nanocarbons and transition metal-nitrogen-carbon catalysts for alkaline membrane fuel cells, J. Mater. Chem. A 6 (3) (2018) 776–804.
[21] Y.P. Zhai, B.W. Zhang, R. Shi, S.Y. Zhang, Y. Liu, B.Y. Wang, K. Zhang, G.I. N. Waterhouse, T.R. Zhang, S.Y. Lu, Carbon dots as new building blocks for electrochemical energy storage and electrocatalysis, Adv. Energy Mater. 12 (6) (2022) 36.
[22] A.R. Nallayagari, E. Sgreccia, R. Pizzoferrato, M. Cabibbo, S. Kaciulis, E. Bolli, L. Pasquini, P. Knauth, M.L. Di Vona, Tuneable properties of carbon quantum dots by different synthetic methods, J. Nanostruct. Chem. 12 (2022) 565–580.
[23] L. Tian, Z. Li, P. Wang, X.H. Zhai, X. Wang, T.X. Li, Carbon quantum dots for advanced electrocatalysis, J. Energy Chem. 55 (2021) 279–294.
[24] H.L. Fei, R.Q. Ye, G.L. Ye, Y.J. Gong, Z.W. Peng, X.J. Fan, E.L.G. Samuel, P. M. Ajayan, J.M. Tour, Boron- and nitrogen-doped graphene quantum dots/graphene hybrid nanoplatelets as efficient electrocatalysts for oxygen reduction, ACS Nano 8 (10) (2014) 10837–10843.
[25] Y. Zhao, L.J. Yang, S. Chen, X.Z. Wang, Y.W. Ma, Q. Wu, Y.F. Jiang, W.J. Qian, Z. Hu, Can boron and nitrogen co-doping improve oxygen reduction reaction activity of carbon nanotubes? J. Am. Chem. Soc. 135 (4) (2013) 1201–1204.
[26] T. Van Tam, S.G. Kang, K.F. Babu, E.S. Oh, S.G. Lee, W.M. Choi, Synthesis of B-doped graphene quantum dots as a metal-free electrocatalyst for the oxygen reduction reaction, J. Mater. Chem. A 5 (21) (2017) 10537–10543.
[27] Z.W. Liu, X. Fu, M. Li, F. Wang, Q.D. Wang, G.J. Kang, F. Peng, Novel silicon-doped, silicon and nitrogen-codoped carbon nanomaterials with high activity for the oxygen reduction reaction in alkaline medium, J. Mater. Chem. A 3 (7) (2015) 3289–3293.
[28] F. Li, L. Sun, Y. Luo, M. Li, Y. Xu, G. Hu, X. Li, L. Wang, Effect of thiophene S on the enhanced ORR electrocatalytic performance of sulfur-doped graphene quantum dot/reduced graphene oxide nanocomposites, RSC Adv. 8 (35) (2018) 19635–19641.
[29] R. Sibul, E. Kibena-Poldsepp, U. Maeorg, M. Merisalu, A. Kikas, V. Kisand, A. Treshchalov, V. Sammelselg, K. Tammeveski, Sulphur and nitrogen co-doped graphene-based electrocatalysts for oxygen reduction reaction in alkaline medium, Electrochem. Commun. 109 (2019) 7.
[30] M.L. Di Vona, R. Narducci, L. Pasquini, K. Pelzer, P. Knauth, Anion-conducting ionomers: study of type of functionalizing amine and macromolecular cross-linking, Int. J. Hydrog. Energy 39 (26) (2014) 14039–14049.
[31] M.M. Heravi, M. Ghavidel, L. Mohammadkhani, Beyond a solvent: triple roles of dimethylformamide in organic chemistry, RSC Adv. 8 (49) (2018) 27832–27862.
[32] N.K. Noel, M. Congiu, A.J. Ramadan, S. Fearn, D.P. McMeekin, J.B. Patel, M. B. Johnston, B. Wenger, H.J. Snaith, Unveiling the influence of pH on the crystallization of hybrid perovskites, delivering low voltage loss photovoltaics, Joule 1 (2) (2017) 328–343.
[33] J. Wu, P. Wang, F. Wang, Y. Fang, Investigation of the microstructures of graphene quantum dots (GQDs) by Surface-Enhanced Raman spectroscopy, Nanomaterials 8 (10) (2018) 864.
[34] A. Dychalska, P. Popielarski, W. Frankow, K. Fabisiak, K. Paprocki, M. Szybowicz, Study of CVD diamond layers with amorphous carbon admixture by Raman scattering spectroscopy, Mater. Sci. Pol. 33 (4) (2015) 799–805.
[35] P.N. Thang, L.X. Hung, D.N. Thuan, N.H. Yen, N.T.T. Hien, V.T.H. Hanh, N. C. Khang, J. Laverdant, P. Thu, Temperature-dependent Raman investigation and photoluminescence of graphene quantum dots with and without nitrogen-doping, J. Mater. Sci. 56 (8) (2021) 4979–4990.
[36] E. Dervishi, Z.Q. Ji, H. Htoon, M. Sykora, S.K. Doorn, Raman spectroscopy of bottom-up synthesized graphene quantum dots: size and structure dependence, Nanoscale 11 (35) (2019) 16571–16581.
[37] D.Y. Pan, J.C. Zhang, Z. Li, M.H. Wu, Hydrothermal route for cutting graphene sheets into blue-luminescent graphene quantum dots, Adv. Mater. 22 (6) (2010) 734.
[38] Y.Z. Han, D. Tang, Y.M. Yang, C.X. Li, W.Q. Kong, H. Huang, Y. Liu, Z.H. Kang, Non-metal single/dual doped carbon quantum dots: a general flame synthetic method and electro-catalytic properties, Nanoscale 7 (14) (2015) 5955–5962.
[39] V. Mennella, G. Monaco, L. Colangeli, E. Bussoletti, Raman-Spectra of carbon-based materials excited At 1064 nm, Carbon 33 (2) (1995) 115–121.
[40] G. Ma, G. Ning, Q. Wei, S-doped carbon materials: synthesis, properties and applications, Carbon 195 (2022) 328–340.
[41] M.K. Smith, B.H. Northrop, Vibrational properties of boroxine anhydride and boronate ester materials: model systems for the diagnostic characterization of covalent organic frameworks, Chem. Mater. 26 (12) (2014) 3781–3795.
[42] X.X. Yang, Y.Z. Guo, S. Liang, S.Y. Hou, T.T. Chu, J.L. Ma, X.H. Chen, J.H. Zhou, R. C. Sun, Preparation of sulfur-doped carbon quantum dots from lignin as a sensor to detect Sudan I in an acidic environment, J. Mater. Chem. B 8 (47) (2020) 10788–10796.
[43] M. Hara, P. Joshi, R. Badam, H.H. Huang, M. Yoshimura, Electrocatalytic activity of heteroatom-doped graphene for oxidation of hydroquinones, Electrochemistry 88 (5) (2020) 407–412.
[44] W. Li, M. Zhou, H.M. Li, K.L. Wang, S.J. Cheng, K. Jiang, A high performance sulfur-doped disordered carbon anode for sodium ion batteries, Energy Environ. Sci. 8 (10) (2015) 2916–2921.
[45] Y.F. Wang, L. Li, M. Jiang, X. Yang, X. Yu, L. Xu, One-pot synthesis of boron and nitrogen co-doped silicon-carbon dots for fluorescence enhancement and on-site colorimetric detection of dopamine with high selectivity, Appl. Surf. Sci. 573 (2022), 151457.
[46] L. Nyikos, T. Pajkossy, Fractal dimension and fractional power frequency-dependent impedance of blocking electrodes, Electrochim. Acta 30 (11) (1985) 1533–1540.
[47] A.J. Bard, L.R. Faulkner, Electrochemical Methods: Fundamentals and Applications, 2nd ed., Wiley, New York, 2001.
[48] G.K.H. Wiberg, A. Zana, Levich analysis and the apparent potential dependency of the Levich B factor, Anal. Lett. 49 (15) (2016) 2397–2404.
[49] W.Y. Yan, S.L. Zheng, W. Jin, Z. Peng, S.N. Wang, H. Du, Y. Zhang, The influence of KOH concentration, oxygen partial pressure and temperature on the oxygen reduction reaction at Pt electrodes, J. Electroanal. Chem. 741 (2015) 100–108.
[50] R.E. Davis, G.L. Horvath, C.W. Tobias, The solubility and diffusion coefficient of oxygen in potassium hydroxide solutions, Electrochim. Acta 12 (3) (1967) 287–297.
[51] P.M. Sipos, G. Hefter, P.M. May, Viscosities and densities of highly concentrated aqueous MOH solutions (M+ = Na+, K+, Li+, Cs+, (CH3)(4)N+) at 25.0 °C, J. Chem. Eng. Data 45 (4) (2000) 613–617.
[52] Y. Liu, S. Chen, X. Quan, H. Yu, H. Zhao, Y. Zhang, G. Chen, Boron and nitrogen codoped nanodiamond as an efficient metal-free catalyst for oxygen reduction reaction, J. Phys. Chem. C 117 (29) (2013) 14992–14998.
[53] H. Fei, R. Ye, G. Ye, Y. Gong, Z. Peng, X. Fan, E.L. Samuel, P.M. Ajayan, J.M. Tour, Boron-and nitrogen-doped graphene quantum dots/graphene hybrid nanoplatelets as efficient electrocatalysts for oxygen reduction, ACS Nano 8 (10) (2014) 10837–10843.
[54] S. Wang, E. Iyyamperumal, A. Roy, Y. Xue, D. Yu, L. Dai, Vertically aligned BCN nanotubes as efficient metal-free electrocatalysts for the oxygen reduction reaction: a synergetic effect by co-doping with boron and nitrogen, Angew. Chem. Int. Ed. 50 (49) (2011) 11756–11760.
[55] J. Liang, Y. Jiao, M. Jaroniec, S.Z. Qiao, Sulfur and nitrogen dual-doped mesoporous graphene electrocatalyst for oxygen reduction with synergistically enhanced performance, Angew. Chem. Int. Ed. 51 (46) (2012) 11496–11500.
[56] Y. Su, Y. Zhang, X. Zhuang, S. Li, D. Wu, F. Zhang, X. Feng, Low-temperature synthesis of nitrogen/sulfur co-doped three-dimensional graphene frameworks as efficient metal-free electrocatalyst for oxygen reduction reaction, Carbon 62 (2013) 296–301.
[57] Q. Shi, F. Peng, S. Liao, H. Wang, H. Yu, Z. Liu, B. Zhang, D. Su, Sulfur and nitrogen co-doped carbon nanotubes for enhancing electrochemical oxygen reduction activity in acidic and alkaline media, J. Mater. Chem. A 1 (47) (2013) 14853–14857.